Design and characterization of a pyroelectric detector based on three-dimensional structured hafnium oxide thin films

Robin Lehmkau,[a,*] Doris Mutschall,[a] Alena Kaiser,[a] Martin Ebermann,[a] Nobert Neumann,[a] Malte Czernohorsky,[b] Markus Neuber,[b] Karla Hiller,[c] Jan Seiler,[c] Toni D. Großmann,[d] Alexey Shaporin,[d] and Jens Lienig[e]

[a]InfraTec GmbH, Dresden, Germany
[b]Fraunhofer Institute for Photonic Microsystems (IPMS), Dresden, Germany
[c]TU Chemnitz–Center for Microtechnologies (ZfM), Chemnitz, Germany
[d]Fraunhofer Institute for Electronic Nano Systems (ENAS), Chemnitz, Germany
[e]TU Dresden, Institute of Electromechanical and Electronic Design (IFTE), Dresden, Germany

Abstract. Pyroelectric detectors are used for gas analysis and flame detection because of their fast response and excellent performance. Most pyroelectric devices are based on monocrystalline lithium tantalate or pyroelectric lead zirconate titanate thin films deposited on a silicon (Si) substrate. In comparison, recently discovered pyroelectric-doped hafnium oxide (HfO_2) offers the possibility of manufacturing completely complementary metal-oxide-semiconductor (CMOS)-compatible devices on large Si wafers. This is a promising approach to simplifying mass production of the sensor element and realizing new sensor structures with a high performance. Si substrates were structured with trenches and filled with thin-doped HfO_2 layers by atomic layer deposition to multiply the pyroelectric current responsivity. An effective pyroelectric coefficient of up to 1300 $\mu C/m^2/K$ was measured. Micromechanical structuring of the 6-in Si wafers was used to improve the thermal conversion of the sensor element. The applied plasmonic absorbers increase the infrared light absorption to >80% for the spectral range of 3 to 5 μm, which was determined using Fourier transform infrared reflection measurements. In the first step, the performance of the sensor element was evaluated with an analog transimpedance amplifier with a feedback resistance of 5 GΩ. A specific detectivity $D^* > 1 \cdot 10^7$ cm$\sqrt{\text{Hz}}$/W was measured for the frequency range of 1 to 10 Hz. In addition, an application-specific integrated circuit was designed for the electrical signal conditioning to build a fully CMOS-compatible pyroelectric detector. It offers a simple to manufacture, flexible configuration, and digital communication interface with a signal-to-noise performance close to analog detectors. We present the measurement results of different sensor elements and detector types. [DOI: 10.1117/1.OE.61.12.127102]

Keywords: pyroelectric detector; hafnium oxide; MEMS; CMOS-compatible; thin film; application-specific integrated circuit.

Paper 20220747G received Jul. 7, 2022; accepted for publication Nov. 22, 2022; published online Dec. 12, 2022.

1 Introduction

Pyroelectric detectors are mostly used for high-performance gas analysis and flame detection. There is a constant urge to further improve the detectors regarding signal-to-noise ratio (SNR), miniaturization, and cost-effective mass production. Single crystalline, pyroelectric elements made of lithium tantalate (LT) in a hybrid structure still dominate the market for high-performance applications. The growth and further handling of the LT crystal is an expensive process.

*Address all correspondence to Robin Lehmkau, r.lehmkau@infratec.de

0091-3286/2022/$28.00

A promising alternative is the use of materials that can be fabricated with common complementary metal-oxide-semiconductor (CMOS) semiconductor processes. This enables the design of microstructured silicon (Si)-based sensor elements for best thermal behavior and mass production with cost-effective standard processes on wafer level. Pyroelectric lead zirconate titanate (PZT) thin films were a step forward but do not yet satisfy the requirements of CMOS-compatibility.[1]

Doped hafnium oxide (HfO_2) thin films have been an integral part of semiconductor CMOS technology for the last two decades, and proven processes are the basis for several microelectronic devices, such as memory applications and gate oxides. The unexpected discovery of the pyroelectric and ferroelectric properties of this material system in 2011 has therefore attracted great research interest and has been the subject in numerous scientific publications.[2,3] In particular, the unique material properties enable novel integrated pyroelectric applications. Particular advantages of the HfO_2 material system are the favorable ratio of the pyroelectric coefficient and dielectric permittivity and the established manufacturing processes. In addition, fabrication by atomic layer deposition (ALD) offers the possibility of using three-dimensional, surface-magnified substrates to increase the current sensitivity. In contrast to lead containing PZT, the material is also restriction of hazardous substances compliant, and it can be fabricated on large Si wafers using common semiconductor processes without limitations. The associated advantages are low-cost mass production, reduced effort for packaging and interconnection technology, and the possibility of monolithic integration of electrical readout circuits on-chip. Specifically, the contributions of this paper are the simulation, design, and characterization of the first structured pyroelectric sensor elements based on doped HfO_2. In addition, the performance of the elements is evaluated with both an analog transimpedance amplifier and an application-specific integrated circuit (ASIC) compared with conventional detectors based on LT.

2 Sensor Design

2.1 *Sensor Topology*

The investigations of the pyroelectric layers were carried out on sensitive elements with a surface-structured Si membrane, which is thermally insulated and suspended from the Si frame by means of narrow Si beams (see Fig. 1). The aim of this Si structure is to maximize the temperature change dT/dt of the structured pyroelectric layer due to the incident radiation and achieve a mechanically stable sensor element.

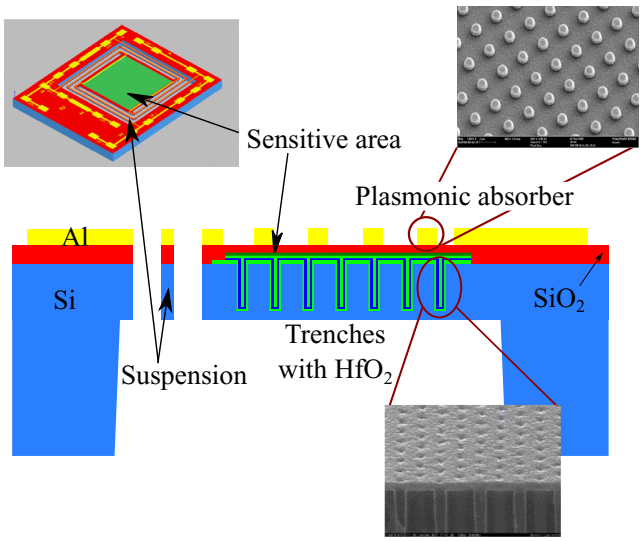

Fig. 1 Overview and schematic cross section of the sensor element with an active area of $\sim 1 \cdot 1\ mm^2$.

An effective surface area A increase by a factor of 10 to 15 is achieved as a consequence of the deep-etched trenches in the membrane arranged in a checkerboard pattern with a high aspect ratio (up to 20:1). The resulting pyroelectric current i_p according to

$$i_p = p \cdot A \cdot \frac{dT}{dt} \tag{1}$$

with the pyroelectric coefficient p is scaled by the same factor. A plasmonic absorber realized by structured aluminum is added to improve the absorption of the incident heat flux and further increase the output signal.

2.2 *Simulations*

The design of the structures was accompanied by extensive simulations. Analyses of the mechanical stability (vibration and shock) with the finite element method (FEM) software *ANSYS* and the thermal behavior with *COMSOL Multiphysics* led to different design variants for the membrane suspension. The aim was to optimize thermal resistance, sensitive area, and mechanical stability while maintaining the same outer dimensions.

Figure 2(a) shows a simulation result of a specific design for a load in the form of a static acceleration of 5000 m/s^2. Maximum stresses (von Mises stress) and tensions at critical points are below 100 MPa, which are low enough to ensure the mechanical stability of the sensor element.[4] Furthermore, the spatial temperature distribution is also illustrated in Fig. 2(b) with a magnitude of up to 2.5 mK for the chosen input flux of 1 W/m^2. The dominating thermal conduction paths are the Si beams, but the surrounding air has to be considered as well, especially for thin membranes below 25 μm. Because of the low thickness and volume of other layers such as HfO_2 or the titanium nitride (TiN) electrodes of just several 10 nm, only Si is considered to be material for the membrane in the FEM model. In Sec. 3, the sensor technology is described in more detail.

With the FEM model, the thermal time constant τ_{th} and the temperature change ΔT of the pyroelectric volume can be calculated in steady state for different membrane thicknesses,

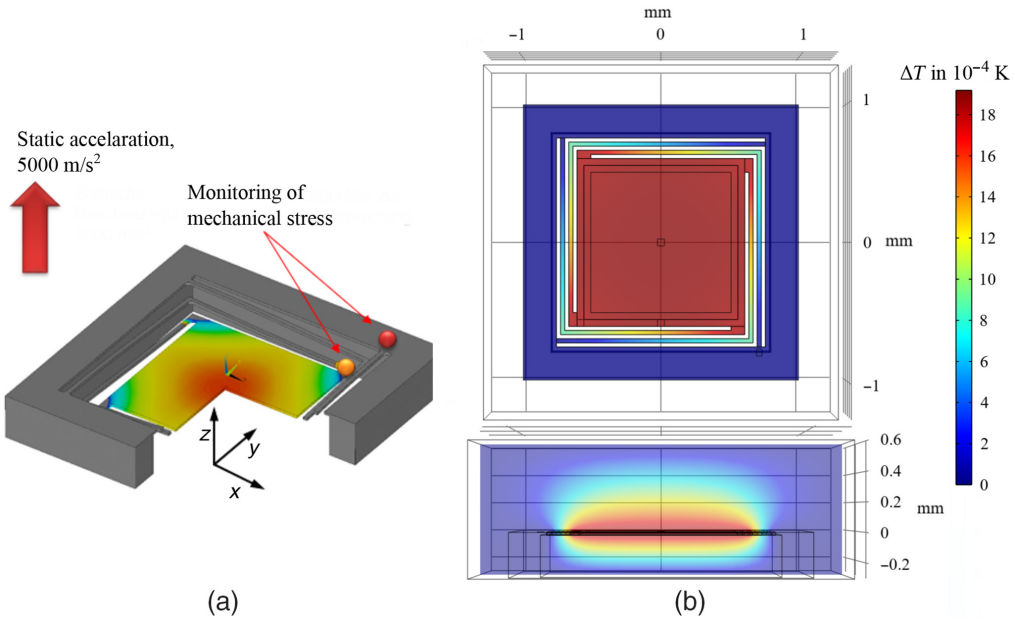

Fig. 2 (a) Deflection (max. 25 μm) and deformation (max. 200 nm) of a sensor membrane with 20 μm thickness for an acceleration of 5000 m/s^2 in the z-direction in *ANSYS*. (b) Steady state of the spatial temperature distribution under consideration of the air environment for an input heat flux of 1 W/m^2 in *COMSOL Multiphysics*.

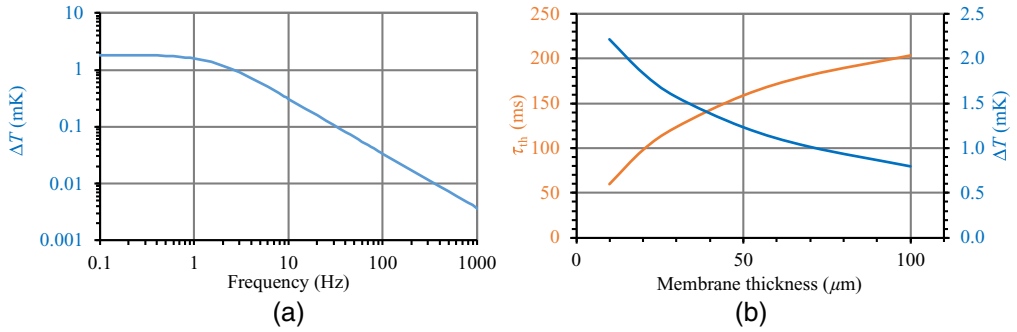

Fig. 3 (a) Temperature sensitivity over excitation frequency of a membrane with a thickness of 20 μm and a thermal time constant of circa 100 ms for an input flux amplitude of 1 W/m^2. (b) Thermal time constant τ_{th} and temperature change ΔT in steady state for different membrane thicknesses.

which are shown in Fig. 3(a). In addition, the frequency dependency of the temperature change can be examined to optimize both thermal capacitance and resistance to the ambience for a specific frequency because a pyroelectrical sensor must always be thermally modulated. A thin membrane with small Si beams and wide gaps is favorable for reducing the thermal mass and increasing the temperature sensitivity.

Due to the pyroelectric effect, a temperature change of the pyroelectric material leads to the generation of electrical charge on its surface, which can be amplified afterward. To simplify the FEM model and to reduce the calculation time and complexity, dividing the pyroelectrical system into thermal and electrical domains with the temperature change $\Delta T(f)$ as the transfer parameter is a useful approach. In the electrical domain, an arbitrary circuit simulation software is used to evaluate the combination of the sensor element with any electrical amplifier. Detailed procedures to model the temperature change and the amplifier in SPICE are explained in Refs. 5 and 6. The frequency dependent output noise and voltage responsivity are simulated with *LTSpice*. Figure 4 shows the simulation results, where the voltage responsivity R_v at 10 Hz of the detector corresponds to a current responsivity R_i of the three-dimensional (3D) (planar) HfO_2 element of $3.05 \cdot 10^{-5}$ A/W ($1.42 \cdot 10^{-6}$ A/W).

For the best thermal behavior and highest responsivity, it is crucial to absorb as much input radiation as possible. The spectral absorption of the plasmonic absorber was optimized using the simulation software *CST Microwave Studio*®. Four absorber types that differ in shape and layer structure were selected for the experimental realization (see Fig. 5). To simplify and accelerate the manufacturing, the CMOS-compatible aluminum metallization for the wiring and pad formation was added with the plasmonic absorber in one deposition step. The limitation is that only a rougher structure with a minimum height down to 700 nm can be realized.

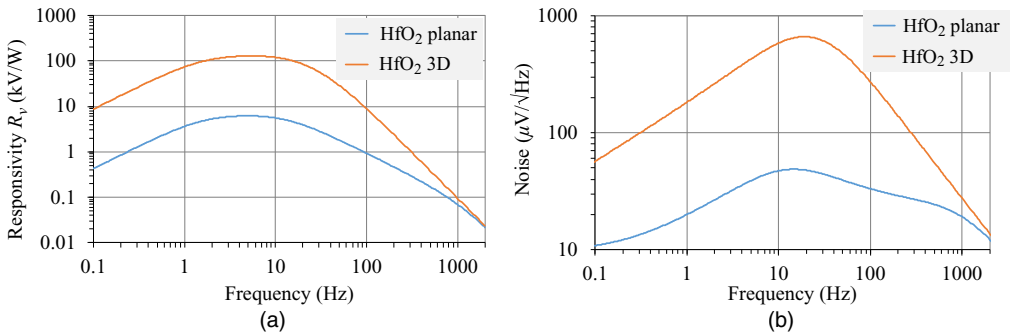

Fig. 4 Simulated (a) voltage responsivity and (b) noise density of a planar and 3D HfO_2 element for a 120 transimpedance amplifier with 5 GΩ||2.5 pF.

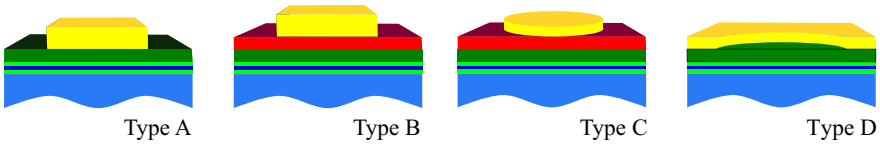

Fig. 5 Realized variants of the plasmonic absorber consisting of aluminum squares or circles on SiO_2 (red) at type B and C and aluminum square or circular aperture directly on the upper HfO_2 electrode (dark green) at type A and D. The lower electrode is connected to Si (blue).

3 Sensor Technology

Two different sensor types were manufactured. The first type has a planar pyroelectric layer of doped HfO_2 as reference, and the second type includes a 3D structured layer for surface enlargement. As additional step for 3D elements, reactive ion etching was used to realize the trench patterning of the Si substrates. Afterward, the pyroelectric layer of doped HfO_2 was conformally deposited using ALD. Doping with Si, aluminum, and lanthanum oxide was achieved by two special refinements of the ALD process. Alternating layers of HfO_2 and Si, aluminum, or lanthanum oxide were deposited in the correct stoichiometric ratio via so-called supercycles. In the second method, the precursors of HfO_2 and the respective doping oxide were mixed in the same ALD cycle.[7]

The electrode material is TiN. It was deposited before and after the pyroelectric HfO_2 layer by chemical vapor deposition on the whole membrane including the trenches. TiN has a low specific resistivity down to $2.2 \cdot 10^{-6}$ Ωm for a low series resistance of the sensor element and builds a proven material stack with HfO_2 and Si regarding the layer tensions and stability of the manufacturing process.[8] The controlled crystallization of the HfO_2 layer by a heat treatment plays a central role because only the non-centrosymmetric, orthorhombic crystal phase of the HfO_2 shows the desired pyroelectric properties. The trench structures are subsequently filled with doped polycrystalline Si. Details of the fabrication processes have been described in the literature.[3]

Finally, electrical contacts as well as the plasmonic infrared absorber structures are fabricated in a common step using SiO_2 for isolation and a 700-nm-thick aluminum metallization. After thinning the wafers back to a thickness of 300 μm, the deep reactive ion etching (DRIE) of the back side is performed to create the thin membranes and pre-etch the separation trenches. Subsequently, a second DRIE process is used to structure the suspensions from the front side to the perforation, with the back side being coated with a protective photo resist. The etching profile in the area of the membrane tapers slightly from the outer frame toward the center of the membrane, which is shown by the cross sections in Figs. 6(a) and 6(b). So far, membranes in the range of 20 to 35 μm in thickness were realized.

Due to the relatively large etch depth, the measured membrane thickness scatters ~10 μm across the wafer and decreases toward the edge of the wafer. Achieving a better homogeneity is the goal of further optimization. Figures 6(c) and 6(d) show detailed views of the realized sensors after patterning. In this example, the width of the Si beams is nominally 30 μm. The structured chips with released membranes need special processes for separation, e.g., protection of the front side during a conventional sawing process from the backside. In addition, a combination of etch processes and mechanical processes is tested.

4 Detector Design

The performances of the planar and 3D structured HfO_2 sensor elements are first characterized with an analog transimpedance amplifier. The huge electrical sensor capacitance ranging from a few to several 100 nF places high demands in terms of noise behavior and signal bandwidth. Simulations supported the dimensioning of the electrical input stage. Subsequently, chosen sensor elements are combined with an ASIC to build a CMOS-compatible pyroelectric detector.

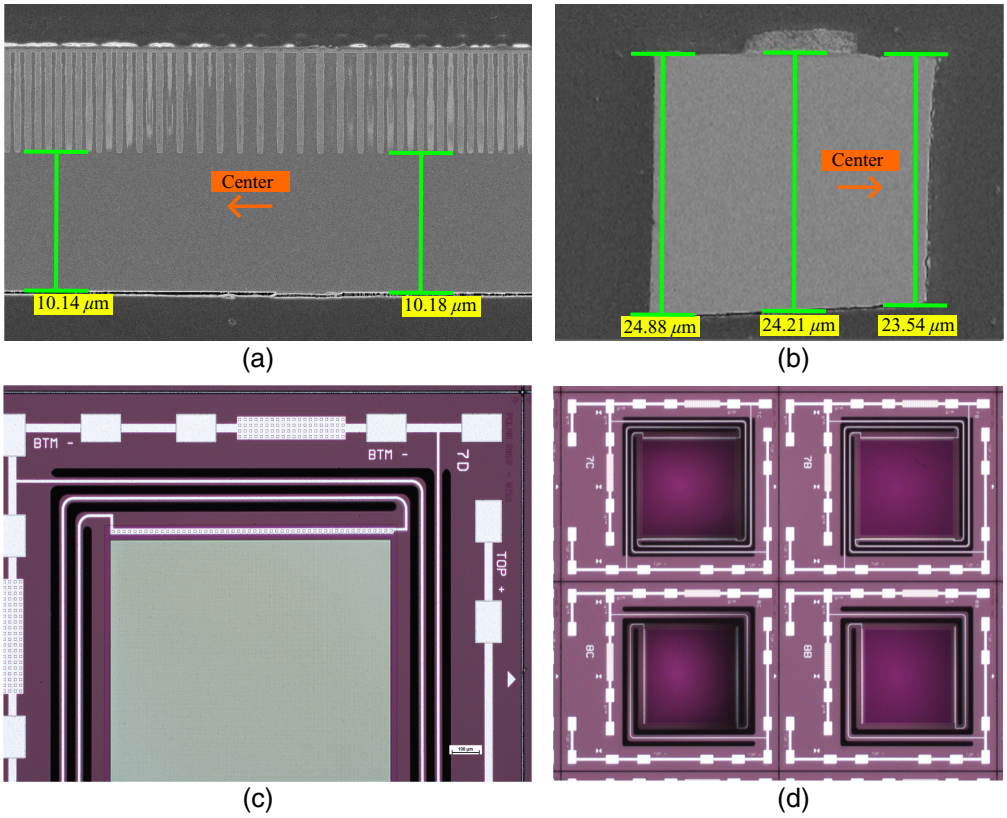

Fig. 6 Scanning electron microscope micrographs: (a) cross section of the membrane and (b) cross section of the feed line. Photos of structure details: (c) front side view after separation and (d) front side view of four sensor elements in wafer composite.

4.1 *Analog*

In comparison with conventional sensors made of LT, the capacitance of the new HfO_2 sensor elements is up to three orders of magnitude higher. For the analog version, a transimpedance amplifier with feedback parameters $R_f = 5$ GΩ and $C_f = 0.4$ pF is used. The realized detector with an equivalent electrical circuit is shown in Fig. 7 for a single measurement channel.

There are several noise sources limiting the performance of a pyroelectric detector. The most important ones are the amplified input voltage noise of the operational amplifier, the tan δ-noise

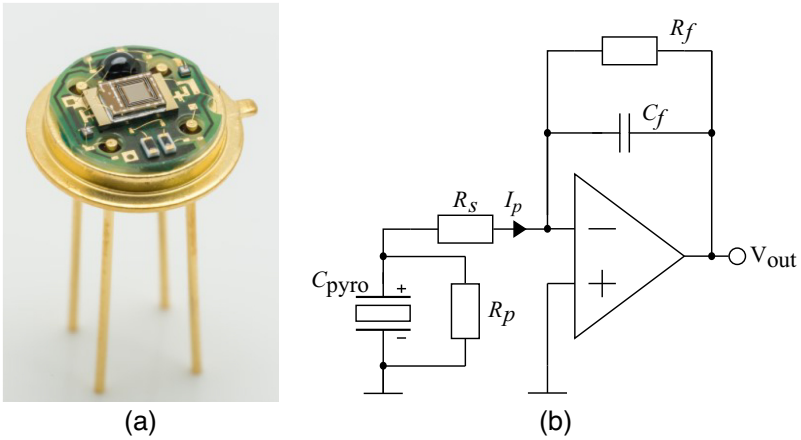

Fig. 7 (a) Analog detector design with HfO_2 sensor element on a TO39 socket. (b) Integrated transimpedance amplifier with sensor capacitance (C_{pyro}), parallel resistance (R_p), series resistance (R_s), feedback resistance (R_f), and feedback capacitance (C_f).

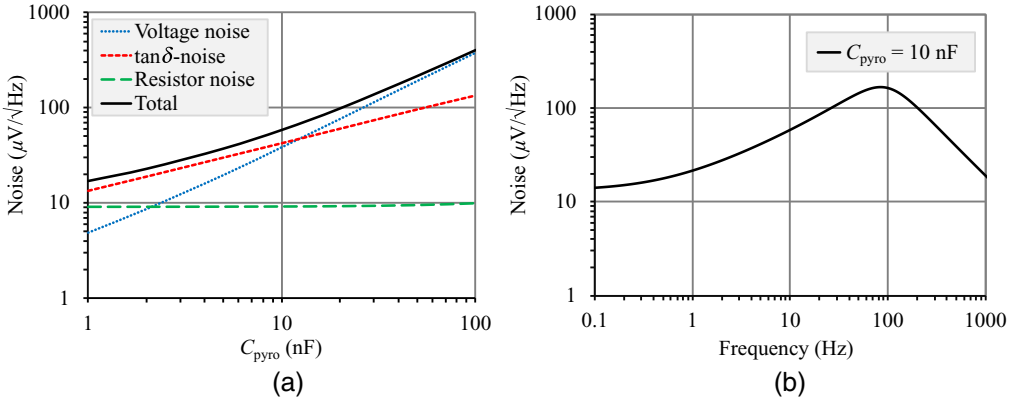

Fig. 8 Simulation of output noise depending on (a) the sensor capacitance C_{pyro} at 10 Hz and (b) the modulation frequency for a capacitance of 10 nF. The feedback parameters are 5 GΩ‖0.4 pF.

of the nonideal sensor capacitance, and the thermal noise of the feedback resistance.[9] *LTSpice* was used to model the noise behavior depending on the frequency and the sensor capacitance C_{pyro}. The thermal noise $u_V = \sqrt{4 \cdot k_B \cdot T \cdot R_f}$ of the feedback resistor R_f is flat white noise for the entire bandwidth of the amplifier with the Boltzmann constant k_B and the temperature T. In contrast, the current noise $i_{\tan\delta} = \sqrt{4 \cdot k_B \cdot T \cdot 2\pi f \cdot C_{pyro} \cdot \tan\delta}$ of the nonideal pyroelectric layer depends on the frequency f, the sensor capacitance C_{pyro}, and dielectric loss tangent $\tan\delta$. The input noise of the operational amplifier u_{in} is multiplied by the ratio of the feedback impedance Z_f and the sensor impedance Z_p.[10] For modulation frequencies above the electrical corner frequency f_{cel} (typically several hertz), the amplification of the input voltage noise u_{in} simplifies to

$$u_{out}(u_{in}) = u_{in} \cdot \left(1 + \frac{Z_f}{Z_p}\right) \overset{f \gg f_{cel}}{\rightarrow} \approx u_{in} \cdot \left(1 + \frac{C_{pyro}}{C_f}\right). \tag{2}$$

The simulated noise components and total noise are plotted in Fig. 8(a) for a specified capacitance range including a low noise operational amplifier at 10 Hz. The curve can be divided into three ranges. For low-capacitance sensors <5 nF, all three noise components contribute to the output noise. For a sensor capacitance of 5 to 50 nF, the resistor noise is negligible. For high-capacitance sensors >50 nF, the total noise is dominated by the amplified voltage noise of the operational amplifier. Furthermore, the output noise and individual noise components also depend on the modulation frequency [see Fig. 8(b)].

The advantage of surface enlargement of the HfO_2 elements works mainly up to 50 nF. Here, an effective surface magnification leads to a proportional signal increase according to Eq. (1), whereby the noise does not increase as much. Consequently, the SNR improves. For high sensor capacitances, further surface expansion would also increase the signal and sensitivity, but the noise grows almost proportionally according to Eq. (2); thus no significant SNR improvement can be expected.

4.2 *Digital*

In the next step, the new HfO_2 sensor elements were combined with an ASIC to build the first pyroelectric detector, in which both sensor element and integrated electrical amplifier can be fully manufactured with CMOS-compatible processes. The ASIC includes an analog frontend similar to the transimpedance amplifier (see Fig. 7), whereby it has almost identical signal and noise behavior to that of the analog counterpart. A big advantage of the ASIC is the configurability of several internal components such as the feedback resistance and capacitance. Figure 9 shows the first experimental setup of the ASIC and two HfO_2 sensor elements. The three optional capacitors are used for voltage stabilization.

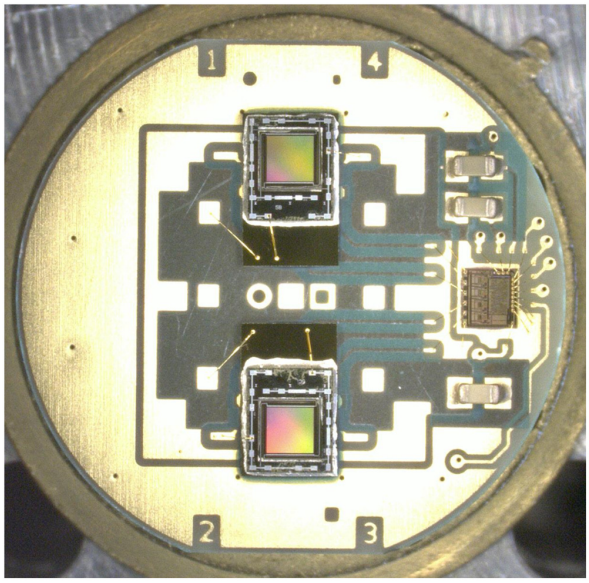

Fig. 9 Preliminary digital detector with two CMOS-compatible HfO_2 sensor elements on a TO8 socket and optional capacitors for voltage stabilization.

5 Measurement Results

5.1 *Sensor Element*

The measurement results of the planar and 3D structured HfO_2 sensor elements are presented in this section. The HfO_2 elements mainly differ in the effective pyroelectric coefficient and electric capacitance depending on the layer thickness, area, and relative permittivity. Table 1 summarizes the properties of HfO_2 with other chosen CMOS-compatible pyroelectric materials and LT as comparison. The 3D structuring of HfO_2 leads to the highest effective pyroelectric coefficient.

In addition to the material parameters, the performance of the deposited plasmonic absorber as part of the sensor element is evaluated. The absorption behavior of the different variants (see Fig. 5) was determined directly in the area of the membrane by means of Fourier transform infrared spectroscopy. For types B and C, a high absorption of >80% was measured over the desired spectral range of 3 to 5 μm, which is illustrated in Fig. 10(a). The shapes of the realized absorber dots in Fig. 10(b) differ from the ideal geometry of a cuboid (type B) and a cylinder (type C). The elements taper toward the top and the edges are rounded due to the fabrication process.

Furthermore, the thermal time constant τ_{th} was measured for a membrane with a total thickness of 22 and 32 μm. Tolerances of material parameters and the manufacturing process lead to a small deviation of <10% between measurement and the simulated values of $\tau_{th} = 95$ and 130 ms, respectively, which are plotted in Fig. 3; these are well suited for most pyroelectric applications.

Table 1 Overview of pyroelectric coefficient and relative permittivity for chosen materials.

Sensor material	Pyroelectric coefficient ($\mu C/m^2/K$)	Relative permittivity
LT	176	47
HfO_2 3D	1300	50
HfO_2 planar	70	50
AlScN[11]	10	10
$BaTiO_3$[12]	200	1200

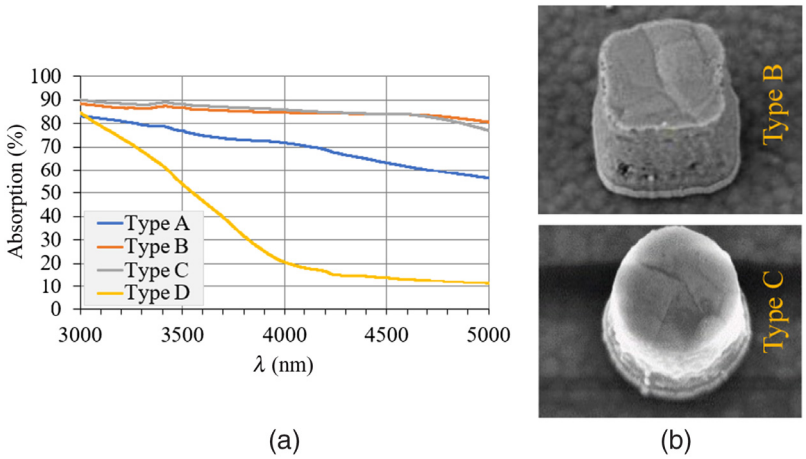

Fig. 10 (a) Measured absorption of different plasmonic absorber types at the spectral range 3–5 μm. (b) SEM micrographs of the absorber types B and C.

5.2 *Analog Detector*

With the current area-enhanced pyroelectric layer and a membrane thickness of 20 μm, a specific detectivity $D^* > 1 \cdot 10^7$ cm$\sqrt{\text{Hz}}$/W (black body 500 K, 3 to 5 μm) in the frequency range of 1 to 10 Hz was achieved with samples (40 nm HfO_2 with Si-doping) from the first development run. The specific detectivity D^* is a common figure of merit for optical detectors and depends on the noise density N, the responsivity R_v, and the sensor area A according to

$$D^* = \frac{R_v}{N} \cdot \sqrt{A}. \tag{3}$$

The enlargement of the effective sensitive pyroelectric area by 3D structuring not only successfully leads to a higher responsivity R_i and R_v (up to a factor of 15) but also amplifies the noise density N at the relevant frequency range, as described in Sec. 4.1. For a growing sensor capacitance above 50 nF, both the signal and noise increase proportionally, in addition to the electrical time constants. Subsequently, high capacitive 3D structured elements only attain a slightly better SNR than planar elements with a capacitance in the range of 10 nF. Figure 11 illustrates the increased noise density of a 3D structured compared with a planar HfO_2 sensor element with the same amplifier.

With the measurement results of the first detector prototypes, two known figures of merit for the material itself are proposed, as shown in Table 2. The goals are, on the one hand, to increase the pyroelectric coefficient p for a high responsivity and, on the other hand, to reduce the permittivity ε and dielectric loss tan δ for a lower noise density. In addition to the material

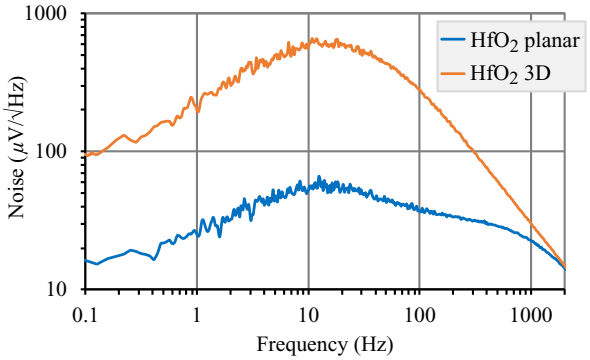

Fig. 11 Noise density of two HfO_2 sensor elements with a planar (≈10 nF) and a 3D structured (≈200 nF) pyroelectric surface combined with an analog transimpedance amplifier (5 GΩ||2.5 pF).

Table 2 Figure of merit for low and high capacitance pyroelectric sensor elements considering a high SNR using a transimpedance amplifier.

Sensor capacitance	Figure of merit
$C_{\text{pyro}} > 50$ nF	$F_{\text{high}} = \frac{p}{\varepsilon}$
$C_{\text{pyro}} \leq 50$ nF	$F_{\text{low}} = \frac{p}{\sqrt{\varepsilon \cdot \tan \delta}}$

parameters, the Si membrane should be as thin as possible to reduce the thermal capacitance, whereas the pyroelectric layer should be as thick as possible to reduce electrical capacitance.

5.3 *Digital Detector*

In this section, the performance of the digital detector including the ASIC is characterized with HfO_2 and state-of-the-art LT elements. As described in Sec. 5.2, the performances of the planar and 3D structured HfO_2 elements are nearly identical, but the capacitance of the planar elements is much closer to the LT elements in the range of several 10 pF. In addition, for the chosen measurement conditions (black body 500 K, 10 Hz, 3 to 5 μm), the high responsivity and capacitance of the 3D structured elements combined with a high feedback resistance would lead to saturation and huge time constants in the input stage. This is why only planar HfO_2 elements are compared with LT with the chosen feedback parameters of the input stage being set to 128 GΩ $\|$ 50 fF to achieve a high SNR.

The measured noise density is shown in Fig. 12(a) for the LT and HfO_2 sensor elements. In Sec. 4.1, the dependency of the output noise on the sensor capacitance is described for a transimpedance amplifier. This is why planar HfO_2 elements with $C_{\text{pyro}} \approx 10$ nF ($d = 40$ nm,

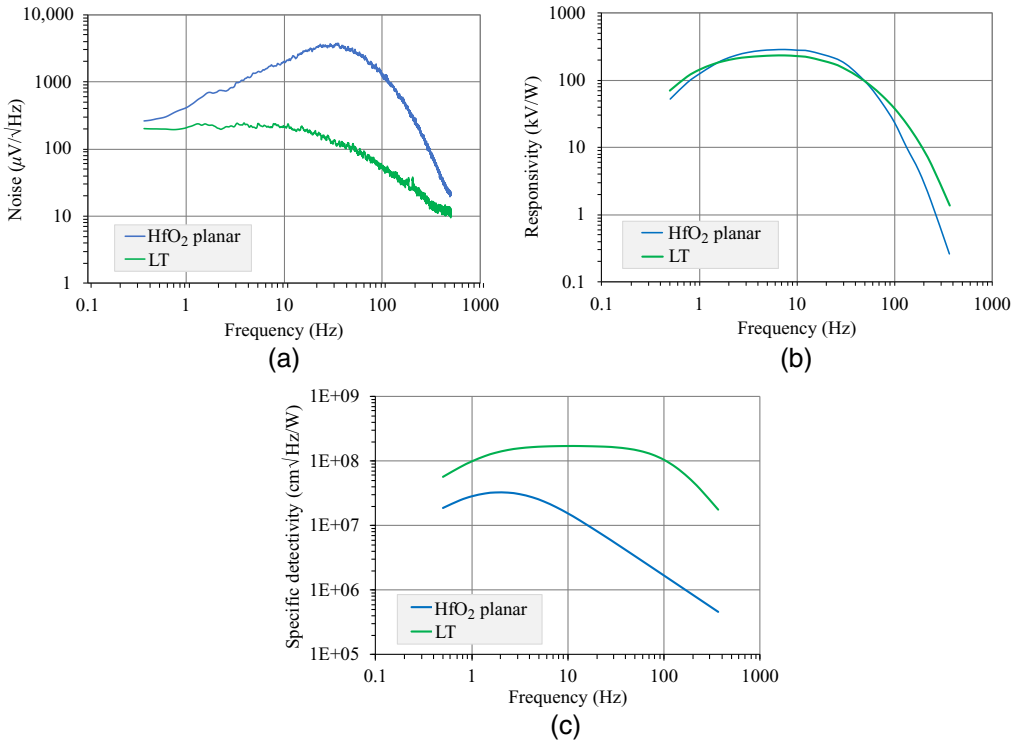

Fig. 12 (a) Measured and fitted noise density, (b) responsivity, and (c) specific detectivity over frequency of a planar 1 mm^2 HfO_2 sensor element with a capacitance of ≈10 nF compared with a conventional 2 mm^2 LT element with a capacitance of ≈0.03 nF. The digital amplification circuit with $R_f = 128$ GΩ $\|$ $C_f = 50$ fF is used.

Table 3 Overview of measured detector parameters for different sensor elements (black body 500 K, 10 Hz, optical filter 3 to 5 μm).

Sensor	Transimpedance amplifier ($R_f \| C_f$)	Sensor area A (mm^2)	Responsivity R_i (A/W)	Noise N (V/$\sqrt{}$Hz)	Detectivity D^* (cm$\sqrt{}$Hz/W)
LT	128 GΩ || 0.05 pF[a]	2.0	$1.9 \cdot 10^{-6}$	$2 \cdot 10^{-4}$	$1.6 \cdot 10^{8}$
HfO_2 planar	128 GΩ || 0.05 pF[a]	1.1	$2.4 \cdot 10^{-6}$	$2 \cdot 10^{-3}$	$1.5 \cdot 10^{7}$
HfO_2 3D	5 GΩ || 2.5 pF	1.1	$2.5 \cdot 10^{-5}$	$6 \cdot 10^{-4}$	$2.0 \cdot 10^{7}$
AlScN[11]	/	0.3	$2.0 \cdot 10^{-5}$	/	$\approx 4.2 \cdot 10^{7}$
LRM-244	100 GΩ || 0.2 pF	4.0	$1.6 \cdot 10^{-6}$	$3 \cdot 10^{-5}$	$6.0 \cdot 10^{8}$

[a]Digital ASIC used as amplifier.

$\varepsilon = 50$) cause a higher noise than LT elements with $C_{\text{pyro}} \approx 30$ pF ($d = 25$ μm, $\varepsilon = 47$). In addition, the loss tangent (tan δ) of the pure polycrystalline material HfO_2 is about a factor of 10 higher compared with monocrystalline LT. Overall, the total noise of planar HfO_2 elements is about a factor of 10 higher at 10 Hz than with LT for the same measurement conditions. The main reasons are the higher tan δ and voltage noise due to worse material imperfections and sensor capacitance of HfO_2, respectively.

The current responsivity R_i of planar HfO_2 elements is about 25% higher at 10 Hz compared with LT because of the optimized thermal sensor design [see Fig. 12(b)]. Due to the successful increase of the effective pyroelectric coefficient, the current responsivity R_i of the 3D structured HfO_2 is more than 10 times higher than for LT and is higher than other state-of-the-art CMOS compatible sensor elements, e.g., based on AlScN with a thin membrane. But in total, the specific detectivity of the HfO_2-detector is lower than of the LT-detector. A comparison of the different sensor elements is shown in Table 3, including the analog commercial detector LRM-244.[13]

6 Summary and Outlook

Area enhanced HfO_2-based pyroelectric sensor elements with 3D structured and planar layers on the Si substrate were fabricated via a fully CMOS-compatible process for the first time. The 3D structured HfO_2 layer magnified the sensor surface, effective pyroelectric coefficient, and resulting current responsivity by a factor of up to 15. However, the sensor capacitance increased as well, which led to higher output noise and limited the SNR in combination with a transimpedance amplifier. A specific detectivity of $D^* \approx 2 \cdot 10^7$ cm$\sqrt{}$Hz/W at 10 Hz was measured for a 40-nm-thick Si-doped HfO_2 element in an analog detector. There is still a performance gap to state-of-the-art detectors using LT, but the prototypes can already be used for applications with lower signal-to-noise requirements such as gas measurements with low resolution. This work showed the potential of HfO_2 regarding the CMOS-compatible manufacturing and high current responsivity. For lower noise and a higher specific detectivity, the sensor capacitance needs to be reduced. A promising approach is to increase the layer thickness of the HfO_2 thin films.

From today's perspective, the fabrication in common Si technology is thus also possible on 12-in (300 mm) wafers, which offers the possibility of cost-effective mass production. No additional effort is required for the broad-band absorber of the infrared radiation because it is produced together with the electrode metallization.

For the first time, a pyroelectric detector with both a sensor element and ASIC was fully manufactured with CMOS-compatible processes, integrated in a small transistor outline package, and successfully put into operation. In addition, the ASIC enabled further miniaturization, allowed for flexible configuration, improved electromagnetic compatibility, and simplified system embedding. The digital detector with the HfO_2 elements reached a detectivity $D^* \approx 1.5 \cdot 10^7$ cm$\sqrt{}$Hz/W at 10 Hz close to the analog counterpart with HfO_2 and a transimpedance amplifier. With monocrystalline LT, a specific detectivity $D^* > 1.6 \cdot 10^8$ cm$\sqrt{}$Hz/W was achieved, which indicates that the sensor element has much bigger potential for optimization than the

amplifier. During the ongoing project, further improvements are planned regarding the sensor structure, plasmonic absorber, and membrane thickness to enhance the thermal and electrical behavior and thus the specific detectivity D^*. Moreover, the integration of both the sensor element and amplifier on a single cost-effective chip with minimum outer dimensions and high performance will be part of future studies.

Acknowledgments

This work was supported by funding from the German Federal Ministry of Education and Research (Grant Nos. 13N15141–13N15144) and is based on the SPIE proceedings paper.[14]

References

1. R. Bruchhaus et al., "A 11 × 6 element pyroelectric detector array utilizing self-polarized PZT thin films grown by sputtering," *Integr. Ferroelectr.* **17** (1–4), 369–376 (1997).
2. J. Müller et al., "Ferroelectric $Zr_{0.5}Hf_{0.5}O_2$ thin films for nonvolatile memory applications," *Appl. Phys. Lett.* **99**(11), 112901 (2011).
3. C. Mart et al., "Layer thickness scaling and wake-up effect of pyroelectric response in Si-doped HfO_2," *Appl. Phys. Lett.* **112**(5), 052905 (2018).
4. A. Fitzgerald and D. Pierce, "Fracture prediction for crystalline microstructures," US20090281768A1 (2009).
5. P. Ramos et al., "A simple thermal and electrical model of an infrared pyroelectric detector using SPICE," *Ferroelectrics* **271**, 379–384 (2002).
6. R. Lehmkau and J. Lienig, "A novel approach to model the thermal-electrical behavior of pyroelectric infrared sensors," in *SMSI 2021 – Sens. And Instrum.*, pp. 177–178.
7. K. Kühnel et al., "High-density energy storage in Si-doped hafnium oxide thin films on area-enhanced substrates," *J. Vac. Sci. Technol. B* **37**(2), 021401 (2019).
8. P. Patsalas et al., "Combined electrical and mechanical properties of titanium nitride thin films as metallization materials," *J. Appl. Phys.* **86**, 5296 (1999).
9. H. Budzier and G. Gerlach, *Thermische Infrarotsensoren: Grundlagen für Anwender*, Wiley-VCH Verlag, Berlin (2010).
10. S. G. Porter, "A brief guide to pyroelectric detectors," *Ferroelectrics* **33**, 193–206 (1981).
11. D. K. T. Ng et al., "A functional CMOS compatible MEMS pyroelectric detector using 12%-doped scandium aluminum nitride," *Appl. Phys. Lett.* **117**, 183506 (2020).
12. Y. Zhang et al., "Thermal energy harvesting using pyroelectric-electrochemical coupling in ferroelectric materials," *Joule* **4**(2), 301–309 (2020).
13. InfraTec GmbH, "Datasheet LRM-244," https://www.infratec.de/downloads/en/sensor-division/detector_data_sheet/infratec-datasheet-lrm-244-_.pdf (accessed 9 May 2022).
14. R. Lehmkau et al., "Fully CMOS-compatible pyroelectric infrared detector based on doped HfO2 thin film in 3D-integration," *Proc. SPIE* **12002**, 120020M (2022).

Robin Lehmkau received his diploma degree in electrical engineering from Technical University of Dresden in 2017. Since 2017, he has been working as a development engineer at InfraTec GmbH in Dresden. Simultaneously, he is pursuing a PhD as an external doctoral student at the Institute of Electromechanical and Electronic Design (IFTE). His research interests are primarily in the modeling, construction, and control of new high-performance pyroelectric detectors in the field of infrared sensors.

Biographies of the other authors are not available.